AGU PUBLICATIONS

JGR

Journal of Geophysical Research: Oceans

RESEARCH ARTICLE

10.1002/2015JC010722

**Key Points:**
- A numerical model describes splitting of gravity current at a density step
- Simulations confirm the experimental hypothesis of current partition theory
- We extend the results to more extreme gravity current regimes as in the field

**Supporting Information:**
- Supporting Information S1

**Correspondence to:**
A. Cortés,
ccalicia@ugr.es

**Citation:**
Cortés, A., M. G. Wells, O. B. Fringer, R. S. Arthur, and F. J. Rueda (2015), Numerical investigation of split flows by gravity currents into two-layered stratified water bodies, *J. Geophys. Res. Oceans*, *120*, 5254–5271, doi:10.1002/2015JC010722.

Received 12 JAN 2015
Accepted 19 JUN 2015
Accepted article online 23 JUN 2015
Published online 31 JUL 2015



# Numerical investigation of split flows by gravity currents into two-layered stratified water bodies

**A. Cortés[1,2], M. G. Wells[3], O. B. Fringer[4], R. S. Arthur[4], and F. J. Rueda[1,2]**

[1]Department of Civil Engineering, University of Granada, Granada, Spain, [2]Institute of Water Research, University of Granada, Granada, Spain, [3]Department of Physical and Environmental Sciences, University of Toronto Scarborough, Toronto, Ontario, Canada, [4]Department of Civil and Environmental Engineering, Stanford University, Stanford, California, USA

**Abstract** The behavior of a two-dimensional (2-D) gravity current impinging upon a density step in a two-layered stratified basin is analyzed using a high-resolution Reynolds-Averaged Navier-Stokes model. The gravity current splits at the density step, and the portion of the buoyancy flux becoming an interflow is largely controlled by the vertical distribution of velocity and density within the gravity current and the magnitude of the density step between the two ambient layers. This is in agreement with recent laboratory observations. The strongest changes in the ambient density profiles occur as a result of the impingement of supercritical currents with strong density contrasts, for which a large portion of the gravity current detaches from the bottom and becomes an interflow. We characterize the current partition process in the simulated experiments using the densimetric Froude number of the current (*Fr*) across the density step (upstream and downstream). When underflows are formed, more supercritical currents are observed downstream of the density step compared to upstream ($Fr_u < Fr_d$), and thus, stronger mixing of the current with the ambient water downstream. However, when split flows and interflows are formed, smaller *Fr* values are identified after the current crosses the density step ($Fr_u > Fr_d$), which indicates lower mixing between the current and ambient water after the impingement due to the significant stripping of interfacial material at the density step.

## 1. Introduction

Gravity currents entering density stratified water bodies frequently introduce suspended and dissolved particles into the system (sediments, pollutants, salt, nutrients), which can affect the biogeochemical processes in the water ecosystem. Therefore, both understanding the vertical distribution of the gravity currents in the water column and quantifying the fate of contaminants are crucial for managing water quality in freshwater systems [*An et al*., 2012]. Similarly, oceanic gravity currents flowing into the stratified ocean can split at sharp density steps [*Wobus et al*., 2013], and understanding the level at which temperature and salt intrude into ocean basins is important for accurate climate modeling [*Legg et al*., 2009]. In addition, the delivery of sediment to the ocean is largely driven by sediment-laden gravity currents, which are often observed to form interflows in the presence of density stratification, especially for supercritical currents [*Talling et al*., 2013]. A large number of theoretical and experimental studies have been conducted to understand mixing in gravity currents and their interaction with either an ambient linear stratification in a closed basin [*Baines*, 2001; *Fernandez and Imberger*, 2008; *Wells and Nadarajah*, 2009] or with a two-layer stratification, where a well-mixed surface layer is separated by a sharp density step from the deep denser waters [*Monaghan et al*., 1999; *Samothrakis and Cotel*, 2006a, 2006b; *Wells and Wettlaufer*, 2007]. When a gravity current enters a two-layered stratification, two inflow behaviors have been widely studied [*Fischer et al*., 1979]. If the impinging current is lighter than the lower layer, then an intrusion forms on the thermocline ("interflow," Figure 1a); otherwise, the current will intrude at the very base of the basin ("underflow," Figure 1c). What has not been widely studied is the process whereby gravity currents can also split as they impinge upon a density step to form two intrusions (Figure 1b) [*Monaghan*, 2007]. This behavior has been previously observed in laboratory experiments with vertical plumes [*Kulkarni et al*., 1993; *Cotel and Breidenthal*, 1997] and turbidity currents [*Rimoldi et al*., 1996; *De Cesare et al*., 2006]. However, these observations gave no general indication of when splitting gravity currents should occur. *Samothrakis and Cotel* [2006a, 2006b] used

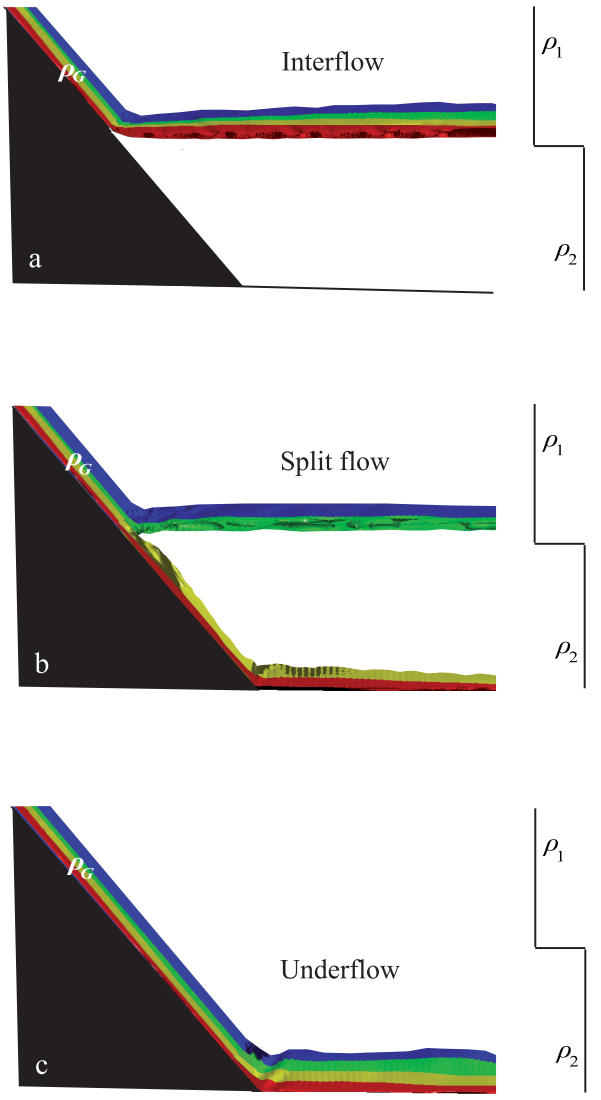


**Figure 1.** Behavior of a 2-D gravity current of average density $\rho_G$ in a two-layered stratified environment, with densities $\rho_1$ and $\rho_2$. The colors represent the internal gradients of density within the gravity current. (a) Interflows occur when $\rho_1 < \rho_G < \rho_2$. (b) Split flows form if the gravity current has significant internal density gradients, and a mean density such that $\rho_G = \rho_2$. (c) Underflows occur if $\rho_G > \rho_2$.

laboratory experiments in two-layered systems to quantify the effects of the impingement on the change in the current velocity across the density step, and proposed empirical relationships to express these velocity differences as a function of the density stratification. *Wobus et al.* [2013] showed in their numerical results the three inflow behaviors (see their Figure 5), and characterized them in terms of the increase in potential energy in the system. Field observations in a Mediterranean reservoir by *Cortés et al.* [2014a] showed that a cold river inflow could split into two intrusions at the base of the surface mixed layer (SML). The latter authors stressed the biogeochemical significance of the formation of near-surface intrusions at a density step, since their entrainment into the top layers of the reservoir could result in fluxes of river-borne nutrients readily used for phytoplankton growth. Thus, it is critical to quantify the portion of gravity currents that could reach the surface layers when entering a stratified system, as well as to understand the conditions controlling the partition of the current at a density step.

Although the splitting of a gravity current when entering a stratified water body has been observed in field, laboratory, and numerical experiments [*Monaghan et al.*, 1999; *De Cesare et al.*, 2006; *Wobus et al.*, 2013], very little has been done to understand why the actual partitioning of the current occurs. The seminal work of *Aagaard et al.* [1985] is one of the earliest references observing the splitting or "shaving" gravity current behavior, by which part of the dense shelf water in the Arctic flowing down the continental margin detached at a variety of depths within the main Arctic basin. They described how the upper portion of the dense down-flow can be continuously mixed with the ambient water until it can "*shave off (or detrained) to interleave along isopycnal surfaces*." The *detrainment* process has been also shown and quantified by *Baines* [2001] through experimental studies in linearly stratified systems. Recent laboratory observations of a two-dimensional (2-D) gravity current flowing downslope into a two-layered stratified system stressed the significance of the gravity current internal properties, as well as the ambient stratification, in determining how a gravity current intrudes into the stratified water body [*Cortés et al.*, 2014b]. The strength of the stratification was quantified in terms of the density Richardson number ($Ri_\rho$) [*Wells and Wettlaufer*, 2007]. For values of $Ri_\rho$ above a given threshold $Ri_\rho$* (~21–27), the gravity current should form an interflow at the density step. For $Ri_\rho < Ri_\rho$*, it should penetrate through the density step forming an underflow. For $Ri_\rho \approx Ri_\rho$*, *Wells and Wettlaufer* [2007] observed that part of the gravity current flowing into the density step would leak to the bottom as an underflow and form multiple intrusions. The internal gradients within the gravity currents can be characterized in terms of the densimetric Froude number ($Fr$). Based on these two nondimensional numbers ($Ri_\rho$ and $Fr$),

*Cortés et al*. [2014b] developed an analytical theory to quantify the portions of the buoyancy flux per unit width from the current that become interflow or underflow (this will subsequently be termed the "flux partition"). They approached this in two ways: (1) experimentally, from the changes in the ambient density profiles observed in a tank after the gravity current injection; and (2) theoretically, based upon the density excess $\Delta\rho(z)$ and velocity gradients $u_G(z)$ within the gravity current. They found that, in general, split flows were likely to occur for supercritical flows ($Fr > 1$) and sharp density steps ($Ri_\rho > 20$–$30$). Despite the good fits between experimental and theoretical estimations of flux partition, there are still sources of uncertainty in their laboratory results, since measuring continuous time series of the study variables (velocity and density) in the whole domain was not feasible in the laboratory. In addition, justification of the actual fate of the gravity current material at a density step, or wider ranges of current regimes could not be tested experimentally. In this regard, numerical modeling is a powerful tool which, once validated, could be used to further investigate the dynamics of gravity currents impinging a density step.

An appropriate solver of mixing processes in small-scale (laboratory) flows [*Zedler and Street*, 2001; *Fringer and Street*, 2003; *Arthur and Fringer*, 2014] is the code developed by *Zang et al*. [1994]. This code employs the nonhydrostatic fractional-step method to solve the Navier-Stokes equations with the Boussinesq approximation with second-order accuracy in time and space using a finite-volume formulation on a curvilinear coordinate (boundary-fitted) grid. Although this code is typically employed as a large-eddy simulation (LES) code using the dynamic-mixed model of *Zang et al*. [1993], computational resources beyond our means were required to resolve the scales of turbulence needed for a true LES of our experiments. Therefore, rather than perform LES, we have replaced the LES subgrid-scale model with a traditional Reynolds-Averaged Navier-Stokes (RANS) approach. Typical RANS models used for environmental flow applications are equivalent, as was shown by *Warner et al*. [2005]. When simulating stratified flows in a salt-wedge estuary, *Wang et al*. [2011a] showed that there was very little difference between three different RANS models (Mellor-Yamada level 2.5, $k$-$\varepsilon$, $k$-$\omega$), but the stability functions which parameterize the effect of stratification had a noticeable effect**.** Given the importance of the stability functions, our strategy is to assume equilibrium turbulence via a balance between production and dissipation, which gives a parabolic turbulent or eddy-viscosity, $\nu_t$. The effects of stratification are parameterized through algebraic expressions in terms of local gradient Richardson numbers $Ri_g$ [*Strang and Fernando*, 2001], that modify $\nu_t$ much in the same way that the stability functions alter the eddy-viscosity in more complex RANS closure schemes. In RANS models, the resolution is dictated by the need to resolve the important vertical gradients, in order to obtain a reasonable prediction of $Ri_g$ needed to parameterize the vertical mixing. *Warner et al*. [2005] presents some test cases for RANS modeling, and the vertical resolution we employ in this work is at least as high as the resolution employed in those cases.

In this study, we employ the parallel Navier-Stokes code by *Cui* [1999], which is the parallel version of the code of *Zang et al*. [1994], to characterize the impinging process of a 2-D gravity current at a density step. Previous laboratory experiments of *Cortés et al*. [2014b] successfully developed a theory to describe the partitioning of the flow, but could not measure all the internal dynamics of gravity currents, and therefore had to make certain assumptions that can now be tested numerically. Furthermore, using the solver we can confirm the validity of the experimental theory over parameter ranges relevant for the ocean and lakes, which are not easily achieved in laboratory. This work is organized as follows. First, we present the available laboratory data, numerical model, and computational setup. Second, we show the model results and confirm the assumptions made in the laboratory to develop the partition theory of the current material at the density step. In the discussion, we evaluate the uncertainties in both the experimental and numerical predictions of flux partition. Then, we characterize the current partition process for a wide range of gravity current regimes through the changes in the densimetric Froude number across the density. Finally, we state the conclusions of our work.

## 2. Methods

### 2.1. Laboratory Experiments and Available Data

In the laboratory experiments of *Cortés et al*. [2014b], a dense 2-D gravity current flowed down a slope of angle $\theta = 25^\circ$ into a rectangular stratified water body, where the initial densities of the two ambient layers were $\rho_1$ in the surface, and $\rho_2$ in the bottom layer (Figure 2). The lower layer was denser than the top layer

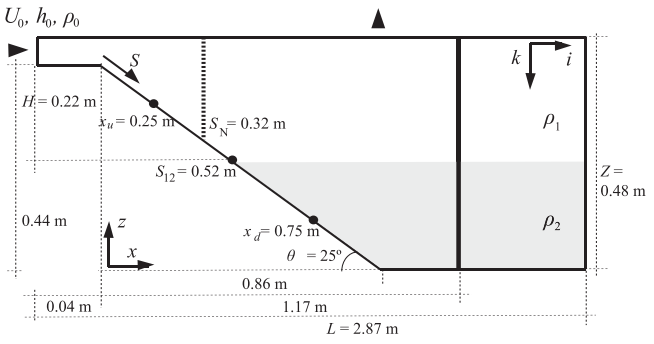


**Figure 2.** Computational domain depicting the dimensions for the simulations corresponding to the 2-D experimental runs (not scaled). The vertical thick solid line marks the location where ambient density profiles were measured ($x$ = 1.17 m). The vertical thick dashed line at the slope ($S_N$ = 0.32 m) marks the location where gravity current profiles where measured. We also mark with dots the location of the density step ($S_{12}$ = 0.52 m), and the cross sections upstream ($x_u$ = 0.25 m) and downstream ($x_d$ = 0.75 m) of $\Delta\rho_{12}$ (Figure 9).

(i.e., $\rho_2 > \rho_1$), and the density step between the layers was defined as $\Delta\rho_{12} = (\rho_2 - \rho_1)$. They also defined $H$ as the vertical distance from the initial depth of the gravity current to the density step, $Z$ as the total depth of the water column, and $L$ as the total length of the tank. Here the coordinate system is relative to the beginning of the ramp, being $x$ the horizontal coordinate relative to the slopeless bottom, $S$ the along-slope coordinate, and $z$ the vertical coordinate. The gravity current, in turn, was initially characterized in terms of its inflow rate $Q_0$, density $\rho_0$, width $W$, inflow reduced gravity $g'_0 = g\ (\rho_0 - \rho_1)/\rho_1$, and its inflow buoyancy flux per unit width $B_0 = g'_0\, Q_0/W$ ($m^3\ s^{-3}$) ($g$ = gravitational acceleration). Tank dimensions and inflow variables were constant in all the experiments, and they are summarized in Table 1. Note that inflow velocity and thickness ($U_0$ and $h_0$) could not be measured in the laboratory. The strength of the stratification was quantified in terms of the density Richardson number ($Ri_\rho$) [*Wells and Wettlaufer*, 2007], calculated as,

$$Ri_\rho = \frac{g'_{12} H}{B_0^{2/3}} \tag{1}$$

where $g'_{12} = g\ \Delta\rho_{12}/\rho_1$ represents the reduced gravity of the ambient water density step. On the other hand, the densimetric Froude number ($Fr$) of the current was calculated from the average velocity $U$, thickness $h$, and reduced gravity $G'$ of the current, as follows,

$$Fr = \frac{U}{(G'h)^{1/2}} \tag{2}$$

where $G' = g\ \Delta P/\rho_1$, and $\Delta P$ ($= \rho_G - \rho_1$) is the average density excess of the gravity current with average density $\rho_G$. The average variables of the gravity current ($h$, $U$, and $G'$) were calculated following *Ellison and Turner* [1959] from the gravity current velocity profile $u_G(z)$ and density excess profile $\Delta\rho(z) = (\rho(z) - \rho_1)$.

**Table 1.** Tank Dimensions and Constant Inflow Conditions of the 2-D Gravity Currents in Laboratory and Simulations

| | | Laboratory | | Simulations | |
|---|---|---|---|---|---|
| Variable | Units | Subcritical | Supercritical | Subcritical | Supercritical |
| *Tank Conditions* | | | | | |
| Length, $L$ | m | 2.5 | | 2.87 | |
| Density of the fresh water, $\rho_1$ | kg $m^{-3}$ | 998 | | 998–1000 | |
| Total water column depth, $Z$ | m | 0.45 | | 0.48 | |
| Thickness of the top layer, $H$ | m | 0.22 | | 0.22 | |
| Thickness of the bottom layer | m | 0.22 | | 0.22 | |
| *Inflow Conditions* | | | | | |
| Inflow rate, $Q_0$ | $m^3\ s^{-1}$ | $8.57 \times 10^{-6}$ | $8.57 \times 10^{-6}$ | $1.08 \times 10^{-5}$ | $1.68 \times 10^{-5}$ |
| Inflow velocity, $U_0$ | $m^3\ s^{-1}$ | N/A | N/A | 0.016 | 0.016 |
| Inflow thickness, $h_0$ | M | N/A | N/A | $3.4 \times 10^{-3}$ | $5.1 \times 10^{-3}$ |
| Inflow density, $\rho_0$ | kg $m^{-3}$ | 1199 | 1199 | 1160 | 1103 |
| Inflow reduced gravity, $g'_0$ | m $s^{-2}$ | 1.97 | 1.97 | 1.568 | 1.009 |
| Inflow buoyancy flux per unit width, $B_0$ | $m^3\ s^{-3}$ | $7.68 \times 10^{-5}$ | $7.68 \times 10^{-5}$ | $7.68 \times 10^{-5}$ | $7.68 \times 10^{-5}$ |

**Table 2.** Specifications of the Simulated Subcritical ($Fr < 1$) and Supercritical ($Fr > 1$) Runs[a]

| Subcritical, $Fr < 1$ | | | Supercritical, $Fr > 1$ | | |
|---|---|---|---|---|---|
| Run | $\Delta\rho_{12}$[b] (kg m$^{-3}$) | $Ri_\rho$[c] | Run | $\Delta\rho_{12}$[b] (kg m$^{-3}$) | $Ri_\rho$[c] |
| A-1 | 64.60 | 77.34 | B-21 | 66.29 | 79.36 |
| A-3 | 51.93 | 62.17 | | | |
| A-4 | 45.88 | 54.92 | | | |
| **A-5** | **34.28** | **41.03** | **B-22** | **38.33** | **45.89** |
| A-10 | 24.28 | 29.07 | B-26 | 24.01 | 28.74 |
| **A-13** | **15.69** | **18.78** | **B-29** | **17.05** | **20.41** |
| A-15 | 9.03 | 10.81 | B-32 | 8.89 | 10.64 |
| **A-17** | **6.15** | **7.36** | **B-34** | **5.32** | **6.37** |
| | | | B-35 | 3.80 | 4.55 |

[a]We mark in bold the experiments whose results are shown in Figure 4.
[b]$\Delta\rho_{12}$—Density difference at the density step.
[c]$Ri_\rho$—Density Richardson number.

The laboratory experiments consisted of two sets of experiments with different gravity current regimes (subcritical with $Fr = 0.69$, and supercritical with $Fr = 1.31$), and the density in the bottom layer ($\rho_2$) was systematically varied in order to attain different $\Delta\rho_{12}$, and thus $Ri_\rho$, since $B_0$ and $H$ were held constant (equation 1). Similar values of $Ri_\rho$ were tested for both subcritical and supercritical gravity currents (Table 2). Both types of currents were achieved by modifying the initial conditions of the inflowing 2-D plume, but conserving the buoyancy flux per unit width at the current.

The available laboratory data to validate model results consist of: (1) density profiles of the ambient water column at the end of the slope ($x = 1.17$ m, Figure 2, thick solid line) measured before and after the injection of the dense current ($\rho_{int}(z)$ and $\rho_{obs}(z)$, respectively) during ~7 min; and (2) velocity $u_G(z)$ and density excess $\Delta\rho(z)$ profiles within the gravity current measured at a site 0.20 m upstream of the density step located at $S_{12} = 0.52$ m (i.e., $S_N = 0.32$ m, Figure 2, thick dashed line). Measured gravity current profiles covered a control volume of 3 cm above the bottom slope with a resolution which ranged between 1 and 0.05 mm for velocity and density, respectively. Here we use equivalent simulated data to apply equations (6)–(12) from *Cortés et al*. [2014b] in order to quantify the flux portions from the simulated current that become interflow and/or underflow ($b_1$ and $b_2$) from both experimental and theoretical approaches.

### 2.2. Numerical Model

The incompressible Navier-Stokes equations for conservation of momentum with the ||Boussinessq approximation, the continuity equation for conservation of mass, and the density transport equation were solved using the nonhydrostatic code developed by *Cui* [1999] in the domain shown in Figure 2. This code employs the fractional-step method of *Zang et al*. [1994] using a finite-volume formulation on a generalized curvilinear coordinate, nonstaggered grid and second-order accurate in both space and time. Momentum advection is accomplished with the QUICK scheme of *Leonard* [1979] and scalar advection is accomplished with the SHARP scheme [*Leonard*, 1987]. This code has been used for many environmental flow applications, including upwelling flow [*Cui and Street*, 2001, 2004], buoyant jets [*Wang et al*., 2011b], sediment transport [*Zedler and Street*, 2001, 2006; *Chou and Fringer*, 2010], internal gravity waves [*Fringer and Street*, 2003; *Arthur and Fringer*, 2014], and internal bolus formation [*Venayagamoorthy and Fringer*, 2007]. Thus, we can assert that this code has been successfully used to study the gravity current hydrodynamics within stratified systems. However, in contrast to these studies which employ the LES technique, we employ a computationally efficient two-dimensional RANS approach which uses roughly 4 times less grid resolution than dictated by LES in our domain (Figure 2). Note that the code requires at least 16 points in the lateral direction because of the multigrid solver, although there is no lateral variability in our calculations. The RANS approach accounts for all of the unresolved turbulence, so inclusion of the third dimension is not needed to resolve the essentially two-dimensional laboratory experiments that we study. We will demonstrate the adequacy of our RANS approach to model the laboratory-scale gravity currents and we will show that the RANS code yields simulation results in good agreement with the laboratory data.

In our RANS implementation, we employ a parabolic eddy-viscosity $\nu_t$ as a function of the flow depth $k$ ($= z - Z$) referred to the tank surface by assuming a momentum balance between the horizontal

pressure gradient and turbulent shear stress (zero-equation turbulence closure scheme) in conjunction with the Boussinesq turbulent-viscosity hypothesis as [*Rodi*, 1993],

$$\nu_t(k) = C_\kappa u_\tau \left(\frac{-k}{D_k}\right)(D_k + k) \tag{3}$$

where $C_\kappa$ is the von Karman constant (= 0.41), $k$ is a negative downward distance from the free surface of the domain, and $D_k$ is the depth of each domain column. Following the practice in many RANS models [e.g., *Fringer et al.*, 2006], $u_\tau$ is the friction velocity calculated with ${u_\tau}^2 = C_D\,{u_1}^2$, where $C_D$ is the drag coefficient, $u_1$ is the magnitude of the horizontal velocity in the bottom grid cell. Since the experimental tank surfaces were smooth (acrylic), we assume an average value of $C_D = 0.0015$ which is within the range reported by *Deacon and Webb* [2005].

To model the damping effect of stratification on the eddy-viscosity, we employ the model of *Munk and Anderson* [1948] who modify the parabolic eddy-viscosity from equation (3) using the gradient Richardson number $Ri_g$ and the depth of the system $k$, with,

$$\nu_{t\,|\,\mathrm{mod}}(k) = \nu_t(k) \cdot \left(1 + \beta\, Ri_g(k)\right)^{\alpha} \tag{4}$$

Here $Ri_g = N^2/S^2$, where the buoyancy frequency is $N = [(-g/\rho_0)(d\rho/dk)]^{1/2}$, $S = du/dz$ is the vertical velocity gradient, and $\alpha$ and $\beta$ are experimentally determined constants with given values of $-0.5$ and 10, respectively [*Munk and Anderson*, 1948]. Note that *Strang and Fernando* [2001] proposed different values for the parameters, as $\alpha = -1.5$ and $\beta = 5$. However, results from our simulations where the latter values are used yielded higher root-mean-square error (*RMSE*) [*Jin et al.*, 2000] when comparing laboratory and simulated results. Thus, we keep values of $\alpha = -0.5$ and $\beta = 10$ in our RANS implementation. In addition, turbulent diffusion in the scalar transport equation is parameterized through the eddy-diffusivity $K_t(k)$, using the fundamental relationship,

$$K_t(k) = \frac{\nu_t(k)}{Pr_t} \tag{5}$$

where $Pr_t$ is the turbulent Prandtl number. This parameterization has been applied to model turbulent flows since the earliest work of *Ellison and Turner* [1959] to recent studies [*Bouffard and Boegman*, 2013], which allows modeling significant reduction of the vertical turbulent mixing that occurs in a strongly stratified system. In addition, the turbulent Prandtl number $Pr_t$ has been reported as a direct function of the gradient Richardson number, $Ri_g$ [see *Elliott and Venayagamoorthy*, 2011, Figure 2]. Note that in the experimental gravity currents studied here, it was always observed an average $Ri_g > 0.25$ below the current-ambient interface layer [see *Cortés et al.*, 2014b, Figures 10c and 10f]. Thus, in this work, we use the following parameterization of $Pr_t$ [*Strang and Fernando*, 2001],

$$Pr_t = \frac{5 \cdot \left(1 + 5 \cdot Ri_g\right)^{-1.5} + 0.2}{5 \cdot \left(1 + 5 \cdot Ri_g\right)^{-2.5} + 0.01} \tag{6}$$

where average gradient Richardson number values below the interface are $Ri_g = [3.85, 0.61]$ in the laboratory subcritical and supercritical gravity currents, respectively, which we are aiming to reproduce. As a result, equation (6) yields average values of turbulent Prandtl number $Pr_t \sim [20, 5]$ for each regime, respectively. According to this parameterization, turbulent scalar mixing is enhanced in supercritical gravity currents (lower $Ri_g$ values).

### 2.3. Computational Setup

The 2-D tank geometry $(l_i, l_k) = (2.86, 0.48)$ m is discretized using a number of grid cells $(n_i, n_k) = (256, 128)$ in the longitudinal, and vertical direction, respectively (Figure 2). Note that the length and height of the simulated domain is larger than in the laboratory experiments, since no water exists below the sloping bottom in the simulated runs (Table 1). Each model run simulates the continuous injection of a dyed gravity current over a period of 7 min with a time step of 0.003 s, resulting in a maximum Courant number of $\sim$0.16. Model results consist of time-evolution of velocity, density, and a passive tracer saved every 6 s or every 2000 time steps.

Prior to the injection of the gravity current, the initial velocity field is quiescent and the initial background two-layered stratification is given by,

$$\frac{\rho}{\rho_1}(k)=1-\frac{\Delta\rho_{12}}{2\rho_1}\tanh\left[\frac{2(k-H)}{\delta_{12}}\tanh^{-1}(\alpha_{12})\right] \quad (7)$$

where $\rho_1 = 1000$ kg m$^{-3}$ is the reference density measured at the top layer with a constant thickness $H = 0.22$ m, $\delta_{12} = 0.03$ m is the interface thickness between the two layers, and $\alpha_{12} = 0.99$ defines the sharpness of the interface. In order to minimize interface thickening due to numerical diffusion, we choose $\delta_{12} \approx 10\Delta k_{Z/2}$, where $\Delta k_{Z/2}$ corresponds to the grid spacing at middepth. In each run (a total of 15), we vary $\Delta\rho_{12}/\rho_1$, defined as the nondimensional density step between the two layers, according to Table 2.

At the left-hand boundary of the domain shown in Figure 2, we prescribe a vertically uniform dense inflow with constant inflow velocity $U_0$, density $\rho_0/\rho_1$, and thickness $h_0$. We vary those values to obtain subcritical and supercritical gravity currents downslope (Table 1), but with the same buoyancy inflow flux per unit width, $B_0 = g\,((\rho_0 - \rho_1)/\rho_1)\,U_0\,h_0$. The reader should note that both $U_0$ and $h_0$ could not be measured in the laboratory, and thus, we have estimated those values in the simulations in order to conserve the experimental value of $B_0$. In addition, we simulate the injection in all currents of a passive tracer with an initial concentration of $C_0 = 1$ kg m$^{-3}$. The right wall is a no-flux boundary, and at the bottom we impose a quadratic drag law with $C_D = 0.0015$, as discussed above. Scalar boundary conditions at all boundaries other than the left boundary are gradient-free. The vertical fluxes at the top boundary are adjusted to conserve mass in the domain (i.e., the inflow flux due to the gravity current on the left boundary is spread along the top boundary as an outflow flux to conserve mass).

We use minimum values of viscosity and diffusivity equal to $\nu = 10^{-5}$ m$^2$ s$^{-1}$, and $K = 10^{-8}$ m$^2$ s$^{-1}$, respectively, in order to account for the fact that density variation in the laboratory experiments was achieved by salinity changes [*Cui and Street*, 2004].

## 3. Results

Simulation results document how both the internal gradients within the gravity current (of average density $\rho_G$) and the strength of the stratification control the fate of the detraining water masses into the ambient. Figure 1a shows that interflows can form when $\rho_1 < \rho_G < \rho_2$, and most of the material flows along the base of the top layer. Split flows occur if the gravity current has significant internal density gradients, and a mean density such that $\rho_G = \rho_2$ (Figure 1b). Underflows form if $\rho_G > \rho_2$, so the majority of the material penetrates the density step and flows along the bottom of the system (Figure 1c). In this section, we first present the results from the numerical model, which we further use to demonstrate the assumptions made in the laboratory to develop the experimental gravity current partition theory at a sharp density step.

### 3.1. Model Validation

The experimental results by *Cortés et al.* [2014b] showed that gravity currents are more likely to detrain into two parts at a density step when they have a diffuse interface layer at the top of the current (supercritical currents), while they tend to intrude as a single intrusion when the current have a sharp, more step-like density profile (subcritical currents). We have successfully reproduced these gravity current patterns using numerical experiments. RANS simulated velocity $u_G(z)$ and density excess $\Delta\rho(z)$ profiles within the gravity current measured at $S_N$ (Figure 2, thick dashed line) exhibit differences which are consistent with those observed in the laboratory at the same location (Figure 3). The supercritical gravity currents have larger values of $h$ and $U$, but lower $\Delta$P than subcritical currents (Figures 3a and 3b). Also, gradients in the density excess profiles tend to be sharper in the subcritical currents, while the current-ambient interface layer is more diffuse and thicker for the supercritical flows (Figures 3c and 3d). Our runs have been able to reproduce a subcritical gravity current ($Fr < 1$) of similar average thickness $h$ and velocity $U$ as in the laboratory, but 31% lower average density excess $\Delta$P, which yields simulated values of $Fr$ slightly higher ($= 0.86$) than in the laboratory (Table 3). On the other hand, simulated supercritical currents ($Fr > 1$) are 5.3% thinner and have 14.9% lower velocity than in the laboratory, but they have similar density excess, resulting in a simulated $Fr$ value smaller ($= 1.10$) than the laboratory (Table 3). These differences between experimental and RANS simulated experiments are likely associated with: (1) the ability to correctly represent entrainment by the described parameterization of *Munk and Anderson* [1948]; and (2) the uniform initial conditions assumed on the west boundary which may not exactly reproduce what was done in the laboratory. In addition, our simulated profiles for both regimes are comparable to the analytical profiles of velocity and density excess

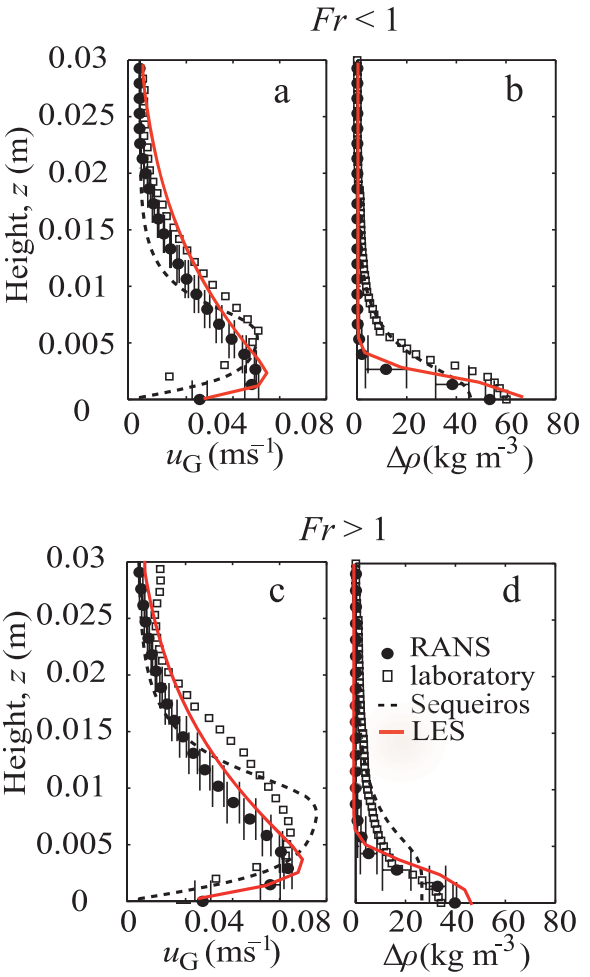


**Figure 3.** Simulated (RANS and LES), experimental, and analytical [*Sequeiros*, 2012] profiles of the two gravity currents gathered at the slope before the current hits the density step ($S_N$), with (a and b) subcritical ($Fr < 1$) and (c and d) supercritical ($Fr > 1$) regimes, where (a and c) are velocity profile, $u_G(z)$, and (b and d) density excess profile, $\Delta\rho(z)$. Error bars mark the standard deviation of the simulated RANS profiles due to the point of measurement at the slope.

determined from the empirical relationships proposed by *Sequeiros* [2012] (Figure 3, dashed lines). Finally, we have found good agreement between the simulated current profiles obtained with our implemented RANS turbulence approach and those reproduced when using the scaled down LES simulations, in which we used a simulated domain where dimensions in all directions were reduced by a factor of 4 (Figure 3, red solid line). Densimetric Froude numbers at the current only change by a maximum of 3.2% depending on the turbulence closure scheme for both current regimes. Thus, we can assume that our RANS implementation in the Navier-Stokes solver of *Cui* [1999] can correctly model the hydrodynamics of the experimental gravity currents in two-layered stratified systems. In addition, we estimated the effective Reynolds number at the gravity current defined as $Re_{gc} = (U\ h)/\nu_t$, where $U$ and $h$ are the simulated average thickness and velocity of the current at the slope (Table 3), and the eddy-viscosity at the gravity current $\nu_t$ was on average of $O(10^{-4})$ m$^2$ s$^{-1}$ (equation (3)). The resulting effective $Re_{gc} \sim 8.5$ in our simulations is much lower than typical field-scale values observed in oceanic currents of $Re_{gc} \sim O(10^7)$, where $h \sim 150$ m, $U \sim 0.5$ m s$^{-1}$, and $\nu = 10^{-6}$ m$^2$ s$^{-1}$ [*Peters and Johns*, 2005; *Fer et al.*, 2010].

Regarding the ambient water density changes, simulated profiles measured at $x = 1.17$ m at the beginning $\rho_{int}(z,\ t = 0$ min) and at the end $\rho_{obs}(z,\ t = 7$ min) of the current injection in a set of numerical experiments show good agreement with experimental results (Figure 4). As in the laboratory, simulated interflows are thicker for larger $Ri_\rho$, since a higher fraction of current flux has been added to the top layer, while for lower values of $Ri_\rho$ underflows tend to increase (for example, Figures 4d and 4f). Furthermore, different gravity current regimes result in different initial and final density profiles for similar $Ri_\rho$, observing larger portions of the inflow current added to the top layer when $Fr > 1$ compared to $Fr < 1$ (for example, Figures 4d and 4a). The major differences between simulated and experimental ambient water density profiles are observed near the density step, likely associated with the numerical diffusion. We quantify the error in the simulated profiles by normalizing the root-mean-square error (*RMSE*) [*Jin et al.*, 2000] by the maximum density value (i.e., $nRMSE = [RMSE\ /\max(\Delta\rho)] \times 100$), which yields maximum values of only $nRMSE \sim 16.6\%$. Finally, both simulated RANS and LES ambient profiles in two runs with different $Fr$ but similar $Ri_\rho$ values are very similar to experimental profiles, which again support the use of our RANS implementation in this work. In summary, the successful comparison of numerical and experimental measurements justifies the further use of the numerical model to confirm the experimental buoyancy flux partition theory.

### 3.2. Buoyancy Flux Partition From Experimental and Simulated Results

Figure 4 has illustrated good agreement between the simulated and experimental vertical distribution of the material from a 2-D gravity current entering a stratified system. Figure 5 shows the simulated spatial distribution of the tracer concentration in the tank after 7 min injection of the two simulated gravity currents

**Table 3.** Average Gravity Current Properties From Laboratory and Simulations Results for the Two Current Regimes (Subcritical $Fr < 1$, and Supercritical $Fr > 1$)[a]

| | | $h$[b] (cm) | $U$[c] (cm s$^{-1}$) | $\Delta P$[d] (kg m$^{-3}$) | $Fr$[e] |
|---|---|---|---|---|---|
| Laboratory | Subcritical | 1.68 | 3.3 | 14 | 0.69 |
| | Supercritical | 2.06 | 5.1 | 8 | 1.31 |
| Simulations and analytical | Subcritical | 1.61 | 3.36 | 9.5 | 0.86 |
| | Supercritical | 1.95 | 4.34 | 8.1 | 1.1 |

[a]We use the same values as in the simulations to dimensionalize analytical profiles by *Sequeiros* [2012].
[b]$h$—Average thickness of the gravity current (g.c.).
[c]$U$—Average velocity of the g.c.
[d]$\Delta P$—Average density excess of the g.c.
[e]$Fr$—Densimetric Froude number of the g.c.

($Fr < 1$ in Figures 5a and 5c, and $Fr > 1$ in Figures 5b and 5d) into a two-layered stratified system with different density step ($Ri_\rho \sim 42$ in Figures 5a and 5b, and $Ri_\rho \sim 7$ in Figures 5c and 5d). As in the laboratory experiments, we observe thicker interflows for larger values of $Ri_\rho$ (compare Figures 5a and 5c), and also in response to supercritical currents (compare Figures 5b and 5a).

Regarding the partition of the current material, Figure 6 shows good agreement between the laboratory and simulated buoyancy flux portions as a function of the density Richardson number ($b$ versus $Ri_\rho$) for the two types of gravity current regimes. Note that simulation results yield similar estimations of buoyancy flux portions from the two approaches, which use simulated ambient density changes and simulated gravity current profiles, respectively. Nevertheless, simulated and experimental results associated to similar values of $Fr$ and $Ri_\rho$ have a maximum difference of 16.8%. This difference is more obvious in the supercritical current regime (Figures 6b and 6d). For instance, the maximum $Ri_\rho$ value required for a pure interflow, named

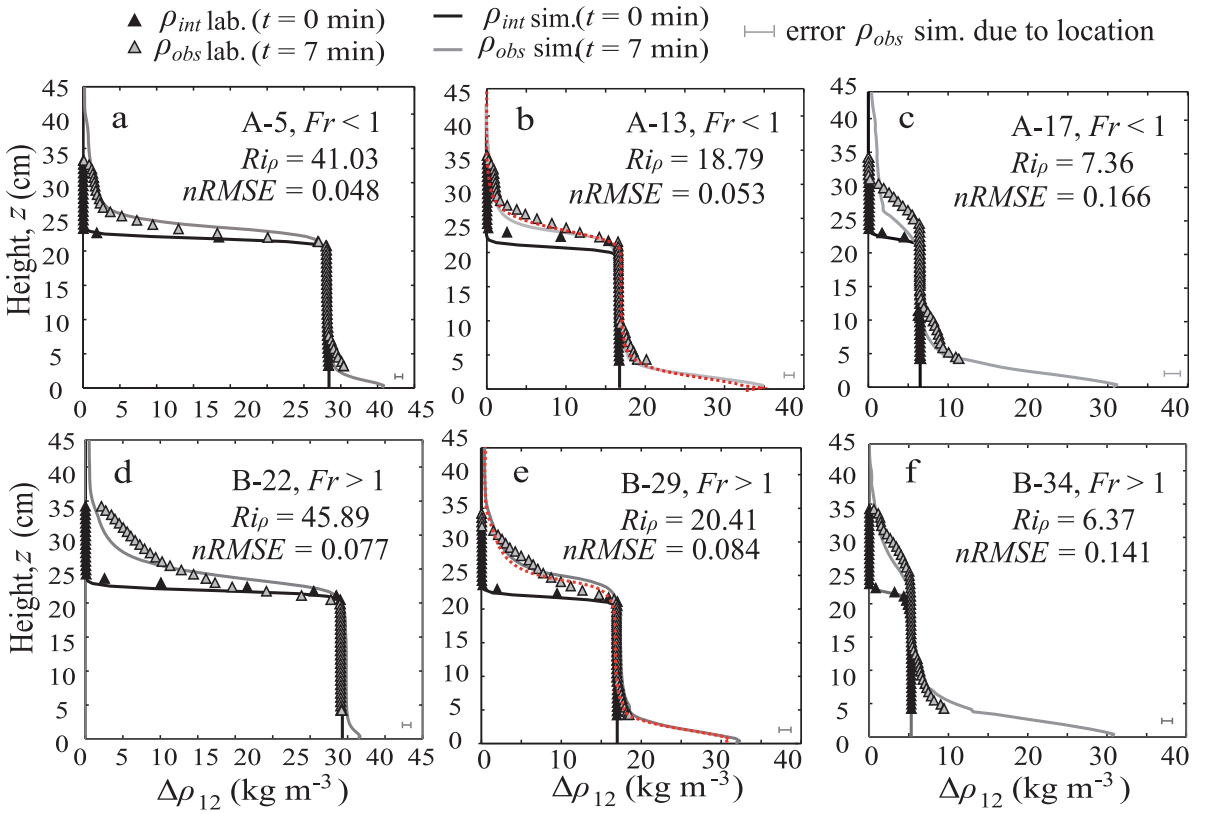


**Figure 4.** Experimental (lab.) and RANS simulated (sim.) ambient water density profiles before the gravity current injection ($\rho_{int}$) and after ~7 min since the beginning of the injection ($\rho_{obs}$), gathered at $x = 1.17$ m in the tank (Figure 2) during the experiments mark in bold in Table 2. Maximum standard deviations in the simulated profiles (due to the point of measurement in the tank) are marked in the lower right corner of the graph with horizontal bars. Values of the normalized *RMSE* (*nRMSE*), *Fr*, and $Ri_\rho$ are also included in each subplot. We also added LES final ambient profiles in two runs (red dashed lines).

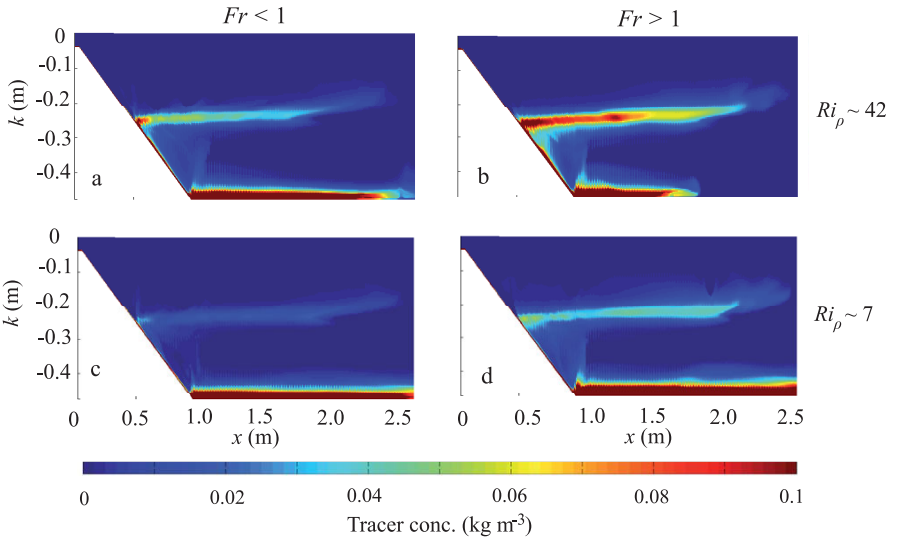


**Figure 5.** Simulated spatial distribution of the tracer concentration (conc.) in the tank after 7 min of injection of the two simulated gravity currents: (a and c) subcritical and (b and d) supercritical, into a stratified system with different density step (a and b) $Ri_\rho \sim 42$ and (c and d) $Ri_\rho \sim 7$.

$Ri_\rho^*$ (i.e., $b_1(Ri_\rho^*) = 1$), is 12.5% larger in our supercritical simulations, while it is the same value both in experimental and simulated results from the subcritical regime. The difference is likely due to the fact that we could not reproduce a more accurate representation of the internal gradients of the gravity currents observed in the laboratory (i.e., different *Fr*). However, simulation results provide complete time and spatial series of velocity and density excess, which allow us to confirm assumptions made in the laboratory to develop the partition theory of the current material at the density step, which could not be demonstrated in the laboratory.

We have simulated the injection of different tracers within the vertical profile of the gravity current in order to demonstrate that there is a height at the current $z = z_i$ such that $\Delta\rho(z) = \Delta\rho_{12}$, which divides the injected current buoyancy flux in two portions ($b_1$ and $b_2$). Thus, at $t = 2$ min (experiments marked in bold in Table 2), we simulate the injection of two pulses of different tracers (named, $C_1$ and $C_2$) with the same concentration ($= 2$ kg m$^{-3}$) during a period of 1 min. Both tracers are injected at the same longitudinal location ($S_N = 0.32$ m), but throughout a different set of cells in the vertical direction: $C_2$ from the bottom to $z_i$, and $C_1$ between $z_i$ and the top of the current (defined by $h$). Figure 7 shows the simulated tracer concentration distribution of $C_1$ and $C_2$ by the end of the pulse injections ($t \sim 3$ min), for the two studied gravity currents (subcritical in Figures 7a and 7c, and supercritical in Figures 7b and 7d) and similar density steps, $Ri_\rho \sim 20$. For both current regimes, higher concentrations of $C_1$ are observed flowing along the density step (Figures 7a and 7b), while $C_2$ values are larger along the bottom of the system (Figures 7c and 7d). As a result, we observe by the end of the pulse injections a maximum of 89% of the injected mass by tracer 1 retained at the density step ($C_1$, standard deviation of 9%), while we measure up to 81% of the injected mass by tracer 2 flowing along the bottom of the tank ($C_2$, standard deviation of 5%). Thus, we can confirm the assumptions made in the experimental partition theory based on the internal gravity current gradients as physically possible.

## 4. Discussion

The numerical simulations are able to give us more insight into the physical process that characterize the current partition using densimetric Froude number changes across the density step. We have shown that the flux partitioning is well modeled by the numerical simulations, even though we have identified some uncertainties. Thus, now we use further simulations to cover a wider range of gravity current regimes than those studied in the laboratory, and include more field-relevant values of *Fr*.

### 4.1. Sources of Uncertainty

Two sources of error in the buoyancy flux portion estimations were identified in the laboratory: (1) the measurement location of the density excess $\Delta\rho(z)$ and velocity $u_G(z)$ profiles within the gravity current at the

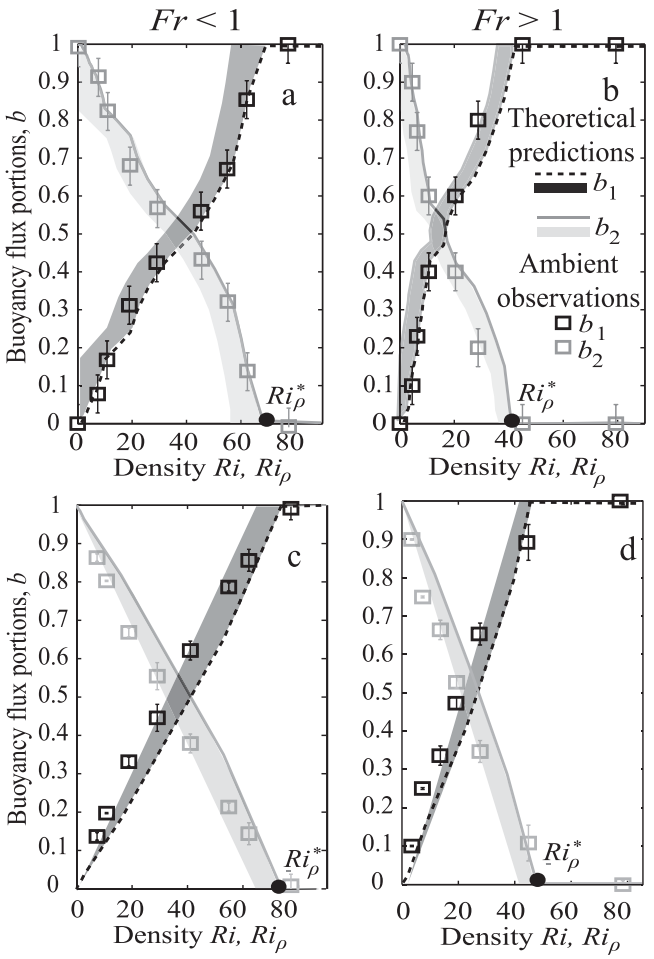


**Figure 6.** (a and b) Laboratory and (c and d) simulated buoyancy flux portions as a function of the density Richardson number ($b$ versus $Ri_\rho$) for the two types of gravity current: (a and c) subcritical ($Fr < 1$) and (b and d) supercritical ($Fr > 1$). Portions flowing as interflows and underflows are named $b_1$ and $b_2$, respectively. Portions from current profiles are marked with lines (theoretical predictions), while portions from ambient density changes in the tank (ambient observations) are represented by squares. The black dot marks the critical value of $Ri_\rho^*$. The shaded regions show the range of predicted values of $b$ due to the error associated with the measurement location of current profiles at the slope (Figure 2). Vertical lines on top of squares represent the maximum standard deviation in the portion values due to errors associated to the location of the ambient density measurements in the tank.

slope ($S_N = 0.32$ m) before reaching the density step ($S_{12} = 0.52$ m, Figure 2), and (2) the measurement location of the ambient density changes ($x = 1.17$ m). Due to restrictions in the laboratory, *Cortés et al.* [2014b] showed only one characteristic profile at each location. However, in this work, we use simulation results to evaluate the possible errors in the buoyancy flux portion estimates when profiles are taken over a range of $S$ and $x$ locations at the slope and further from the ramp, respectively. Horizontal error bars in Figures 3 and 4 represent the maximum standard deviation of profiles gathered over a given range ($S = [0.32 - 0.5]$ m, and $x = [1.17 - 1.67]$ m). As a result, vertical error bars and shaded regions in Figures 6c and 6d show uncertainty of simulated $b$ values, which ranged between 0.1 and 10%.

In addition to the errors associated with the location of profile measurements, simulation results have inherent numerical errors or uncertainties. Thus, model performance evaluation is crucial in assessing modeling efficacy [*Bennett et al.*, 2013]. A complete analysis of uncertainty in the simulation can be found as a supporting information document associated with this paper. Herein, we focus on the errors associated with the vertical resolution, which we observed to significantly affect the modeled gravity current hydrodynamics.

Numerical simulations by *Legg et al.* [2006] suggested that coarse resolutions could cause excessive mixing within the downslope current. Our simulation results support this argument, since larger portions of the current buoyancy flux are retained at the density step as an interflow ($b_1$) for the same pair of $Fr$ and $Ri_\rho$ values

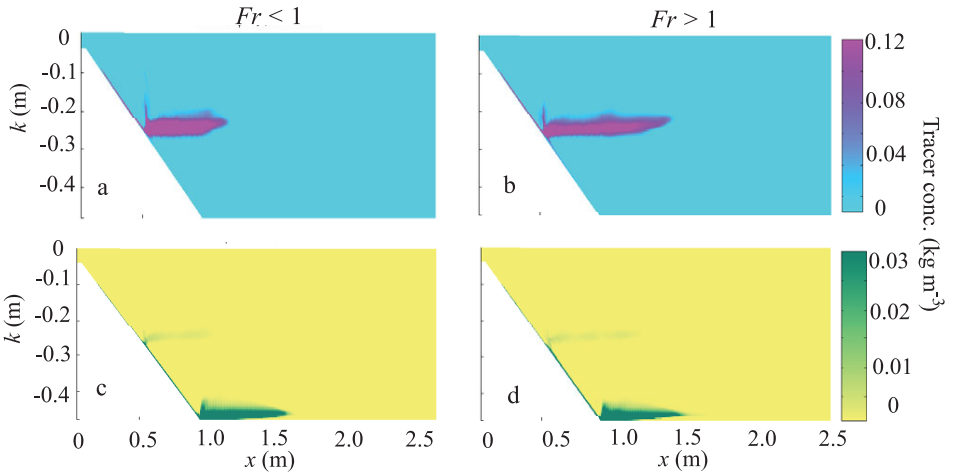


**Figure 7.** Simulated spatial distribution of the two pulses of different tracers ($C_1$ and $C_2$) injected into different vertical locations at $S_N$ after 3 min release of the two gravity currents, (a and c) subcritical and (b and d) supercritical, into a stratified system with a density step $Ri_\rho \sim 20$. Concentration of the tracer injected at the top of the current ($C_1$) is shown in Figures 7a and 7b, while concentration of the tracer injected at the bottom of the current ($C_2$) is shown in Figures 7c and 7d.

at coarser vertical resolutions ($n_k = 32$ and 64) than when using the actual (and finer) vertical grid spacing chosen in this study, $n_k = 128$ (Figure 8). In addition, experimental portions of $b_1$ measured in the laboratory are almost coincident with those simulated considering $n_k = 128$ (Figure 8, compare with dashed lines), justifying our choice of $n_k$. Furthermore, we have performed an additional set of simulations with finer vertical resolution, $n_k = 256$, which show similar $b_1$ to those yielded by runs with $n_k = 128$ (Figure 8). This confirms the effectiveness of the turbulence model in controlling the observed mixing. We also observe larger increments of simulated $b_1$ portions with coarser resolution when the supercritical currents ($Fr > 1$) enter weak stratified water columns ($Ri_\rho \sim 7$). As a result, we should carefully define the vertical resolution of the simulated domain in order to provide a correct representation of the inflow behavior and its partition when entering a two-layered system. Assuming that simulation results yield the sort of errors described in this

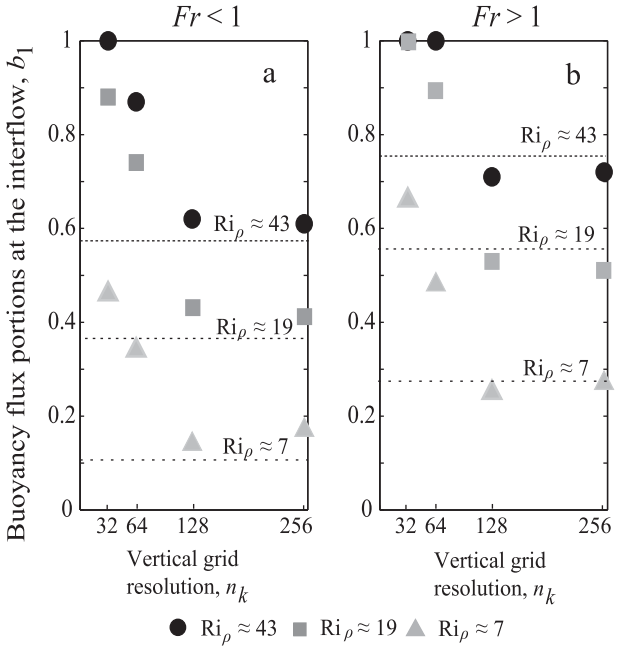


**Figure 8.** Uncertainty in the estimations of the buoyancy flux portion flowing as an interflow ($b_1$) as a function of the vertical grid cells ($n_k$). Results are shown from the injection of two different current regimes (subcritical in 8a and supercritical in 8b) into a stratified system with density step $Ri_\rho$. The dashed lines mark the experimental portion $b_1$ measured in the laboratory for each pair of values $Fr$ and $Ri_\rho$.

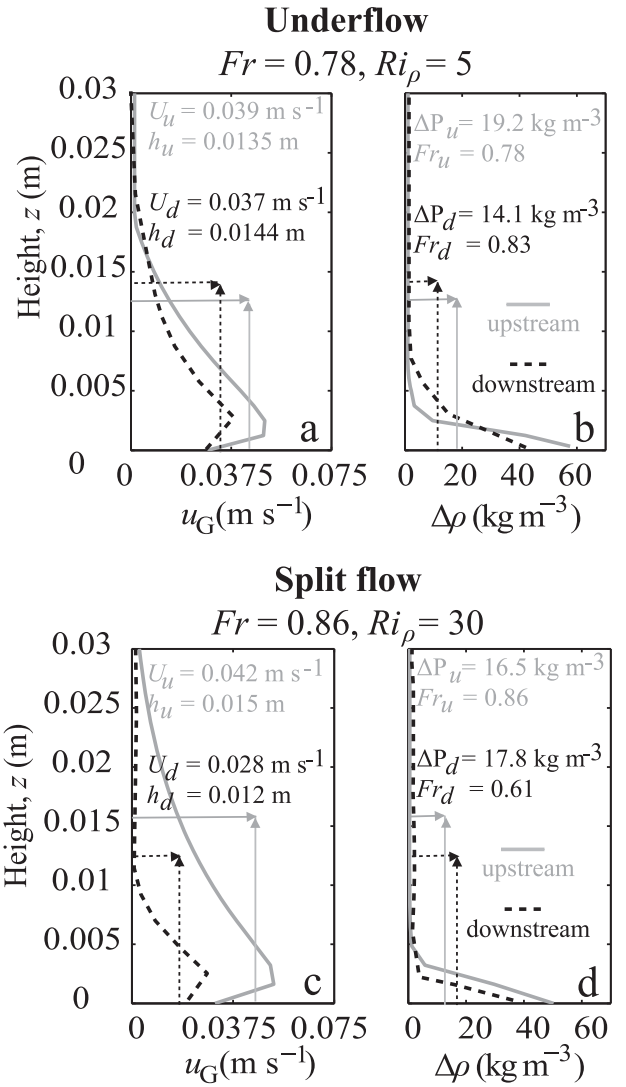


**Figure 9.** Vertical profiles of (a and c) velocity $u_G(z)$, and (b and d) density excess $\Delta\rho(z)$ at two different locations in the slope (Figure 2): upstream ($u$) and downstream ($d$) of the density step ($S_{12}$). Each horizontal pair of plots corresponds to a different run with characteristic $Fr$ and $Ri_\rho$ values and gravity current behavior: (a and b) underflow when $Fr_u = 0.78$ and $Ri_\rho = 5$; (c and d) split flow when $Fr_u = 0.86$ and $Ri_\rho = 30$. We also mark the average properties at the current (thickness $h$, velocity $U$, density excess $\Delta P$, and Froude number $Fr$) for each experiment and location.

section, we will now use the model to characterize the impinging process of a wider range of gravity current regimes ($Fr$) and stratification strengths ($Ri_\rho$), which are likely to find in lakes and the ocean.

### 4.2. Behavior of Gravity Currents With Extreme Regimes

A wide range of published field measurements [*Peters and Johns*, 2005; *Arneborg et al.*, 2007; *Fer et al.*, 2010] have shown more dramatic velocity and density vertical gradients within gravity currents than those shown in the laboratory currents studied by *Cortés et al.* [2014b]. Here we have run new sets of simulations where inflow conditions (thickness $h_0$, velocity $U_0$, and density $\rho_0$) are varied but the experimental inflow $B_0$ is kept constant, in order to create gravity currents with more extreme regimes than in the laboratory. As a result, we aim to characterize the effects of the impingement on the vertical structure of five different gravity currents ($Fr$ = [0.61, 0.78, 0.86, 1.1, 1.22]) into five stratifications $Ri_\rho \sim$ [5, 20, 30, 40, 60].

#### 4.2.1. Changes of the Internal Gradients Within the Current Due to Its Impingement

Our simulation results presented in Figure 9 show significant changes of the vertical current velocity $u_G(z)$ and density excess $\Delta\rho(z)$ profiles at two different cross sections located upstream ($x_u = 0.25$ m) and downstream ($x_d = 0.75$ m) of the density step $S_{12}$ (Figure 2). In general, the current reduces its velocity due to the

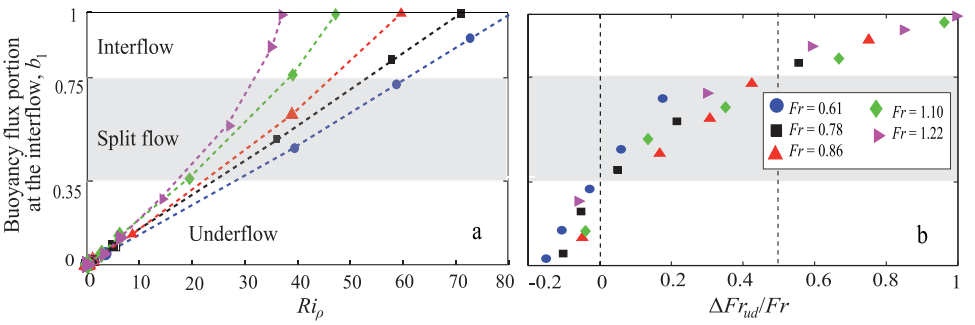


**Figure 10.** Theoretical predictions (from simulated current profiles) of buoyancy flux portions flowing as interflow ($b_1$) as a function of: (a) density Richardson number, $Ri_\rho$, (b) normalized changes of the densimetric Froude number across the density step, $\Delta Fr_{ud}/Fr$. Dashed rectangles mark the range of values of $b_1$ associated with split flows. Different symbols represent different gravity current regimes.

impingement. However, the changes in the variables depend both on the current regime ($Fr$) and density stratification ($Ri_\rho$). For instance, when the current forms underflows after crossing the density step (e.g., Figures 9a and 9b, $Fr_u = 0.78$ and $Ri_\rho = 5$), it suffers both a reduction in the average velocity and density excess ($\Delta P_u = 19.2$ kg m$^{-3} > \Delta P_d = 14.1$ kg m$^{-3}$), while the current becomes thicker downstream ($h_u = 1.35$ cm $< h_d = 1.44$ cm). As a result, the modified current after $S_{12}$ presents a $Fr_d$ larger than upstream ($Fr_u = 0.78 < Fr_d = 0.83$). However, when a split flow is observed in our simulations (e.g., Figures 9c and 9d, $Fr_u = 0.86$ and $Ri_\rho = 30$), the average current density excess increases when crossing the $\Delta\rho_{12}$ ($\Delta P_u = 16.5$ kg m$^{-3} < \Delta P_d = 17.8$ kg m$^{-3}$), while it becomes thinner downstream ($h_u = 1.5$ cm $> h_d = 1.2$ cm), and thus the modified current downstream is characterized by smaller densimetric Froude number than upstream ($Fr_u = 0.86 > Fr_d = 0.61$). As a result, we propose to evaluate the changes of the densimetric Froude number across the density step, in order to diagnose the changes of the current properties due to its impingement depending on the formation of underflows, split flows or interflows in our simulated experiments (Figure 1).

#### 4.2.2. Changes of Densimetric Froude Numbers Across the Density Step

Many field, laboratory and numerical studies of gravity currents have used the densimetric Froude number (or its inverse-related Richardson number, $Ri = Fr^{-2}$) as a measure of the importance of inertial to buoyancy forces [*Dallimore et al*., 2001; *Sequeiros et al*., 2010; *Venayagamoorthy and Fringer*, 2012]. Here we quantified the normalized variation in $Fr$ upstream and downstream of the density step, as $\Delta Fr_{ud}/Fr = (Fr_u - Fr_d)/Fr_u$, in order to evaluate the changes suffered by the current when crossing a density step, and resulting in different vertical distributions of the current material in the ambient water column (Figure 1). In addition, we used the theoretical partition of the inflowing buoyancy flux ($b$ portions) determined by the different simulated current profiles to characterize the different gravity current behaviors. We have assumed that underflows are formed when the theoretical $b_1$ ranges between 0 and 35%, split flows could be observed if $b_1 \sim$ 35–75%, and interflows will be related with $b_1 > 75\%$ (Figure 10a).

We have observed different ranges of the normalized change in $Fr$ across the density step depending on the resulting current behavior (Figure 10b). Underflows are formed in those runs characterized by $\Delta Fr_{ud}/Fr < 0$, since a larger value of the densimetric Froude number is measured downstream $\Delta\rho_{12}$ ($Fr_u < Fr_d$). We associated this fact with the low flow stripping of the lighter interfacial material at the density step, observing a more supercritical current downstream the density step, which presents thicker interface layers at the top of the current and smaller average density excess of the current after it crosses $S_{12}$ ($h_u < h_d$, and $\Delta P_u > \Delta P_d$). All these changes are indicative of a strong mixing of the current with the ambient water downstream.

Split flows and interflows are observed when $\Delta Fr_{ud}/Fr > 0$ (Figure 10b) due to the fact that smaller values of $Fr$ are estimated after $S_{12}$ ($Fr_u > Fr_d$). We relate this observation with a significant stripping of interfacial material at the density step, which results in a downstream current with a thinner interface layer and larger density excess ($h_u > h_d$, and $\Delta P_u < \Delta P_d$). In this case, these observations indicate lower mixing between the current and ambient water after its impingement. We have identified split flows when $\Delta Fr_{ud}/Fr = [0, 0.5]$ and interflows if $\Delta Fr_{ud}/Fr = [0.5, 1]$.

In general, the described differences in $\Delta Fr_{ud}/Fr$ across the density step can be associated with the systematic changes in density profiles. As shown by *Cortés et al*. [2014b, Figure 2], low Froude number flows have less diffuse velocity and density gradient than high Froude number flows. This is driven by the increase in

interfacial entrainment rates as a function of Froude numbers [*Ellison and Turner*, 1959; *Cenedese and Adduce*, 2010]. We have estimated the entrainment coefficient as the change in the average current thickness downslope, $E = \mathrm{d}h/\mathrm{d}S$ [*Ellison and Turner*, 1959], which yields different values of $E$ depending on the measurement location respect to $S_{12}$ (upstream and downstream) and the observed current behavior. The current described in Figures 9a and 9b (forming an underflow) yields $E_u = 0.058$ and $E_d = 0.062$, while the current associated with the split flow (Figures 9c and 9d) shows $E_u = 0.064$ and $E_d = 0.046$. Thus, higher levels of mixing between current-ambient after the impingement water are expected when underflows are formed ($Fr_u < Fr_d$) while lower mixing downstream is quantified when we observe split flows or interflows ($Fr_u > Fr_d$).

## 5. Conclusions and Implications

We have shown that the vertical distribution of a 2-D gravity current entering a stratified system is critical to determining how material is portioned upon encountering a sharp density step. Simulated results reproduce recent experimental observations of buoyancy flux partition, which quantify the portion of a gravity current which flows as interflow and/or underflow after its impingement with a density step. In addition, our simulation results show good agreement with laboratory data on reproducing both: (1) the internal gradients of the two study gravity current regimes (characterized by the densimetric Froude number, $Fr$, as subcritical and supercritical), and (2) the change in the ambient stratification of the two-layered system (with different stratification strengths or density Richardson number, $Ri_\rho$) after the injection of the dense inflow. The physical validation of the modified parallel nonhydrostatic Navier-Stokes' solver of *Cui* [1999] with our implementation of a zero-equation turbulence model, allowed us to (1) successfully confirm, through tracer experiments, the experimental assumptions of buoyancy flux partition of the gravity current suggested in the laboratory, and (2) evaluate errors in the analytical partition theory due to both the measurement location of the available laboratory data, and numerical uncertainties associated with the vertical resolution of the computational domain. According to simulation results, changes in the locations where laboratory data were gathered did not significantly modify the predicted portions of the current that flows as interflow or/and underflow after impinging a sharp density step. Regarding numerical uncertainties, we found that vertical resolution is the key parameter to determining the internal structure of gravity currents, and hence their splitting behavior. Of secondary importance is the exact form of parameterizing diffusivity as a function of Richardson numbers, as we found only small differences between using constant values from *Munk and Anderson* [1948] versus *Strang and Fernando* [2001]. In addition, particular attention should be taken for the simulation of supercritical currents into weakly stratified systems, since the lower the resolution, the larger the portion flowing as interflow, even tending to hide the actual splitting of the current.

Our simulations are very relevant for many natural lakes where relatively weak density steps can develop at the thermocline. For example, in Mediterranean stratified reservoirs during the late summer-early fall. *Cortés et al*. [2014a] observed small density steps ($\Delta\rho_{12} = 0.07$ kg m$^{-3}$) within the stratified column of Lake Béznar (Spain) by the end of the stratification season (September 2009, see their Figure 5), when they reported the formation of split flows. Similar density steps were also observed in Lake Geneva during the field study of *Halder et al*. [2013, Figure 6] in October 2010, when they used an isotopic analysis of Rhône river water to identify interflows below the surface-mixed layer. Our simulations should motivate more careful field-work to determine if there could be significant flow splitting occurring in cases where any interflows are detected.

We have characterized the current partition process of a wide range of current regimes ($0.61 < Fr < 1.22$) through the changes in the densimetric Froude number across the density step in order to diagnose the changes in the current when crossing $\Delta\rho_{12}$. When underflows are formed, more supercritical currents are observed downstream the density step compared to upstream ($Fr_u < Fr_d$), and thus, strongest mixing of the current with the ambient water has been identified after the impingement. The large values of $Fr$ downstream are associated with thicker interface layers and smaller average current density excess due to the low flow stripping of the lighter interfacial material at the density step.

However, when split flows and interflows are formed, smaller $Fr$ values are identified after the current crosses the density step ($Fr_u > Fr_d$), which indicates lower mixing between the current and ambient water downstream. The formation of more subcritical currents after the impingement is due to the significant

stripping of interfacial material at the density step, which results in a downstream current with a thinner interface layer and larger density excess. As a result, flow stripping at the density step can actually increase the average density excess of the remaining fluid that intrudes below the surface layers. A direct consequence of this observation is that the material flows deeper than expected from just the average properties of the gravity current. *Aagaard et al*. [1985] suggested this point when showing how temperature and salinity relationships of water in the Arctic Ocean changed as the masses flowed deeper.

Large-scale oceanographic gravity currents are highly turbulent and are strongly influenced by Coriolis forces that arise from the Earth's rotation. To gain some understanding of the implications of our results when dealing with highly turbulent currents, we have run new numerical experiments in which a gravity current of $Re_{gc} \sim 10$ entered into a two-layered stratified system with three different density steps ($Ri_\rho \sim$ [5, 10, 20]). The resulting $b_1$ portions flowing as an interflow increased 5–8% compared to those yielded by a previously simulated current with $Re_{gc} \sim 8.5$ (Table 3). These results suggest that highly turbulent oceanic currents with $Re_{gc}$ almost six orders of magnitude larger than our laboratory-scale currents are likely to detrain even larger buoyancy flux portions at a density step than those presented in this study. This trend in increasing entrainment rate with increases in Reynolds number has also been described by *Cenedese and Adduce* [2010] and *Wells et al*. [2010].

The influence of Coriolis forces on oceanographic gravity currents results in changes to the downward trajectory, velocity, and the internal circulation. The deflection of downslope gravity currents due to the Coriolis force in a rotating system is well documented, and in the Northern Hemisphere the deflection is to the right-hand side (looking downstream) so that a curved trajectory will result for gravity currents flowing down on a uniform slope [*Cenedese et al*., 2004; *Davies et al*., 2006]. The Burger number can be used to determine the relative importance of rotation on gravity current dynamics, which is defined as $Bu = (g'_0 H)/(f L)$, where $f$ is the Coriolis parameter. Thus, $Bu$ represents the ratio of the time scale over which rotational effects become important to the advective time scale of the gravity current. Our laboratory-scale simulations clearly yield values of $Bu \gg 1$, and thus we do not consider the effects of rotation on the development of intrusions in our numerical study. However, interflows formed in the ocean or large lakes may have $Bu < 1$.

To first order, oceanographic gravity currents are in a geostrophic balance, and their depth averaged velocity $U$ is reduced in comparison to a similar nonrotating flow [*Nof*, 1996; *Cossu et al*., 2010]. Thus, the Froude number of these geostrophic flows is generally lower than similar nonrotating flows, which implies that there will be lower entrainment rates [*Turner*, 1986; *Wells et al*., 2010]. A reduction in entrainment with increasing rotation rate has also been seen experimentally [*Cenedese et al*., 2004; *Wells and Wettlaufer*, 2007]. Thus, one impact of Coriolis forces is that a smaller fraction of the gravity current flowing as interflow may split at the density step due to the decrease in entrainment, compared to a similar nonrotating gravity current. The presence of entrainment at the upper interface of the gravity current, and drag at the lower boundary, means that oceanographic gravity currents are not in a pure geostrophic balance, and the resulting upper and lower Ekman layers result in a transverse secondary circulation, as reported in the Faroe Bank Channel by *Johnson and Sanford* [1992], and in experimental studies [*Cossu et al*., 2010]. This transverse circulation is at most 10% of the downstream flow, and should not change the basic splitting processes we have discussed in this paper. However, it is likely that this transverse circulation will make subtle changes to the vertical distribution of both density and downstream velocity compared to the nonrotating gravity currents. These changes in secondary circulation and a decrease in the bulk downstream velocity that are both due to Coriolis forces, mean that the predicted partition theory by *Cortés et al*. [2014b] from nonrotating laboratory experiments may need to be modified for use in large-scale quasi-geostrophic gravity currents. Hence, we suggest further numerical work considering more turbulent currents (higher $Re_{gc}$), as well as the influence of the Coriolis force on the exact details of density and velocity profiles, in order to gain more insight into the formation of multiple intrusions in large lakes or the ocean.

The numerical model presented here can be also extended to predict the partition of a wide range of gravity current regimes entering different stratified systems (e.g., linearly density stratified). Our results show that it is critically important to resolve the internal density gradients of the gravity current in order to correctly model mixing. The simulation of excessive mixing would result in the failure to correctly predict the river inflow partition in field settings, which has strong implications for the fate of dissolved substance (e.g.,

nutrients) in the cold river water entering natural water bodies or in dense gravity currents flowing into the deep ocean.

**Acknowledgments**
This work was funded by the Spanish Ministry of Science and Innovation (project CGL2008–06101/BOS). O. B. Fringer and R. S. Arthur gratefully acknowledge the support of ONR grant N00014-10-1-0521 (scientific officers Dr. C. Linwood Vincent, Dr. Terri Paluszkiewicz and Dr. Scott Harper). M. G. Wells acknowledges funding from NSERC. The data of this study are not available online. We thank the IT and Communication Center at the University of Granada (CSIRC) for allowing us to use their super computer *Alhambra*. Specially, we appreciate the help provided by Rafael Redondo during the simulation process. The reader can contact A. Cortés (ccalicia@ugr.es) in order to obtain the data used in this work, since this information is not available online.

## References

Aagaard, K., J. H. Swift, and E. C. Carmack (1985), Thermohaline circulation in the Arctic Mediterranean seas, *J. Geophys. Res.*, *90*, 4833–4846, doi:10.1029/JC090iC03p04833.

An, S., P. Y. Julien, and S. K. Venayagamoorthy (2012), Numerical simulation of particle-driven gravity currents, *Environ. Fluid Mech.*, *12*, 495–513, doi:10.1007/s10652-012-9251-6.

Arneborg, L., V. Fiekas, L. Umlauf, and H. Burchard (2007), Gravity current dynamics and entrainment: A process study based on observations in the Arkona basin, *J. Phys. Oceanogr.*, *37*, 2094–2113, doi:10.1175/JPO3110.1.

Arthur, R. S., and O. B. Fringer (2014), The dynamics of breaking internal solitary waves on slopes, *J. Fluid Mech.*, *761*, 360–398, doi:10.1017/jfm.2014.641.

Baines, P. (2001), Mixing in flows down gentle slopes into stratified environments, *J. Fluid Mech.*, *443*, 237–270, doi:10.1017/S0022112001005250.

Bennett, N. D., et al. (2013), Characterizing performance of environmental models, *Environ. Modell. Software*, *40*, 1–20, doi:10.1016/j.envsoft.2012.09.011.

Bouffard, D., and L. Boegman (2013), A diapycnal diffusivity model for stratified environmental flows, *Dyn. Atmos. Oceans*, *61*, 14–34, doi:10.1016/j.dynatmoce.2013.02.002.

Cenedese, C., and C. Adduce (2010), A new parameterization for entrainment in overflows, *J. Phys. Oceanogr.*, *40*, 1835–1850, doi:10.1175/2010JPO4374.1.

Cenedese, C., J. A. Whitehead, T. A. Ascarelli, and M. Ohiwa (2004), A dense current flowing down a sloping bottom in a rotating fluid, *J. Phys. Oceanogr.*, *34*, 188–203, doi:10.1175/1520-0485(2004)034<0188:ADCFDA>2.0.CO;2.

Chou, Y. J., and O. B. Fringer (2010), A model for the simulation of coupled flow-bedform evolution in turbulent flows, *J. Geophys. Res.*, *115*, C10041, doi:10.1029/2010JC006103.

Cortés, A., M. G. Wells, W. E. Flenoor, I. de Vicente, and F. J. Rueda (2014a), Pathways of river water to the surface layers of stratified reservoirs, *Limnol. Oceanogr.*, *59*, 233–250, doi:10.4319/lo.2014.59.1.0233.

Cortés, A., F. J. Rueda, and M. G. Wells (2014b), Experimental observations of the splitting of a gravity current at a density step in a stratified water body, *J. Geophys. Res. Oceans*, *119*, 1038–1053, doi:10.1002/2013JC009304.

Cossu, R., M. G. Wells, and A. K. Wåhlin (2010), Influence of the Coriolis force on the velocity structure of gravity currents in straight submarine channel systems, *J. Geophys. Res.*, *115*, C11016, doi:10.1029/2010JC006208.

Cotel, A. J., and R. E. Breidenthal (1997), Jet detrainment at a stratified interface, *J. Geophys. Res.*, *102*, 23,813–23,818, doi:10.1029/97JD01695.

Cui, A. (1999), *On the parallel computing of turbulent rotating stratified flows, PhD dissertation*, Stanford Univ., Stanford, Calif.

Cui, A., and R. L. Street (2001), Large-eddy simulation of turbulent rotation convective flow development, *J. Fluid Mech.*, *447*, 53–84, doi:10.1017/S0022112001006073.

Cui, A., and R. L. Street (2004), Large-eddy simulation of coastal upwelling flow, *J. Environ. Fluid Mech.*, *4*, 197–223, doi:10.1023/B:EFMC.0000016610.05554.0f.

Dallimore, C. J., J. Imberger, and T. Ishikawa (2001), Entrainment and turbulence in a saline underflow in Lake Ogawara, *J. Hydraul. Eng.*, *127*, 937–948, doi:10.1061/(ASCE)0733-9429(2001)127:11(937).

Davies, P. A., A. K. Wåhlin, and Y. Guo (2006), Laboratory and analytical model studies of the Faroe Bank Channel deep-water outflow, *J. Phys. Oceanogr.*, *36*, 1348–1364, doi:10.1175/JPO2917.1.

De Cesare, G., J. L. Boillat, and A. J. Schleiss (2006), Circulation in stratified lakes due to flood-induced turbidity currents, *J. Environ. Eng.*, *132*, 1508–1517, doi:10.1061/(ASCE)0733-9372(2006)132:11(1508).

Deacon, E. L., and E. K. Webb (2005), Small-scale interactions, in *Physical Oceanography*, edited by M. N. Hill and A. R. Robinson, Harvard Univ. Press, Cambridge, Mass.

Elliot, Z. A., and S. K. Venayagamoorthy (2011), Evaluation of turbulent Prandtl (Schmidt) number parameterizations for stably stratified environmental flows, *Dyn. Atmos. Oceans*, *51*, 137–150, doi:10.1016/j.dynatmoce.2011.02.003.

Ellison, T. H., and J. S. Turner (1959), Turbulent entrainment in stratified flows, *J. Fluid Mech.*, *6*, 423–448, doi:10.1017/S0022112059000738.

Fer, I., G. Voet, K. S. Seim, B. Rudels, and K. Latarius (2010), Intense mixing of the Faroe Bank Channel overflow, *Geophys. Res. Lett.*, *37*, L02604, doi:10.1029/2009GL041924.

Fernandez, R., and J. Imberger (2008), Time-varying underflow into a continuous stratification with bottom slope, *J. Hydraul. Eng.*, *134*, 1191–1198, doi:10.1061/(ASCE)0733-9429(2008)134:9(1191).

Fischer, H. B., E. J. List, R. C. Y. Koh, J. Imberger, and N. H. Brooks (1979), *Mixing in Inland and Coastal Waters*, 2nd ed., Academic., N. Y.

Fringer, O. B., and R. L. Street (2003), The dynamics of breaking progressive interfacial waves, *J. Fluid Mech.*, *494*, 319–353, doi:10.1017/S0022112003006189.

Fringer, O. B., M. Gerritsen, and R. L. Street (2006), An unstructured-grid, finite-volume, nonhydrostatic, parallel costal ocean simulator, *Ocean Modell.*, *14*, 139–173, doi:10.1016/j.ocemod.2006.03.006.

Halder, J., L. Decrouy, and T. W. Vennemann (2013), Mixing of Rhône River water in Lake Geneva (Switzerland-France) inferred from stable hydrogen and oxygen isotope profiles, *J. Hydrol.*, *477*, 152–164, doi:10.1016/j.jhydrol.2012.11.026.

Jin, K.-R., J. H. Hamrick, and T. Tisdale (2000), Application of three-dimensional hydrodynamic model for Lake Okeechobee, *J. Hydraul. Eng.*, *126*(10), 758–771, doi:10.1061/(ASCE)0733-9429(2000)126:10(758).

Johnson, G. C., and T. B. Sanford (1992), Secondary circulation in the Faroe Bank Channel outflow, *J. Phys. Oceanogr.*, *22*, 927–933, doi:10.1175/1520-0485(1992)022<0927:SCITFB>2.0.CO;2.

Kulkarni, A. C., F. Murphy, and S. S. Manohar (1993), Interaction of buoyant plumes with two-layer stably stratified media, *Exp. Therm. Fluid Sci.*, *7*, 241–248, doi:10.1016/0894-1777(93)90007-6.

Legg, S., R. W. Hallberg, and J. B. Girton (2006), Comparison of entrainment in overflows simulated by z-coordinate, isopycnal and non-hydrostatic models, *Ocean Modell.*, *11*, 69–97, doi:10.1016/j.ocemod.2004.11.006.

Legg, S., et al. (2009), Improving oceanic overflow representation in climate models: The gravity current entrainment climate process team, *Bull. Am. Meteorol. Soc.*, *90*, 657–670, doi:10.1175/2008BAMS2667.1.

Leonard, B. P. (1979), A stable and accurate convective modelling procedure based on quadratic upstream interpolation, *Comput. Methods Appl. Mech. Eng.*, *19*, 59–98, doi:10.1016/0045-7825(79)90034-3.
Leonard, B. P. (1987), Sharp simulation of discontinuities in highly convective steady flow, *NASA Tech. Memo. 100240*, Institute for Computational Mechanics in Propulsion (ICOMP), Lewis Research Center, Cleveland, Ohio.
Monaghan, J. J. (2007), Gravity current interaction with interfaces, *Annu. Rev. Fluid Mech.*, *39*, 245–261, doi:10.1146/annurev.fluid.39.050905.110218.
Monaghan, J. J., R. A. F. Cas, A. M. Kos, and M. A. Hallworth (1999), Gravity currents descending a ramp in a stratified tank, *J. Fluid Mech.*, *379*, 39–69, doi:10.1017/S0022112098003280.
Munk, W. H., and E. R. Anderson (1948), Notes on a theory of the thermocline, *J. Mar. Res.*, *7*, 276–295.
Nof, D. (1996), Rotational turbidity flows and the 1929 Grand Banks earthquake, *Deep Sea Res., Part I*, *43*, 1143–1163, doi:10.1016/0967-0637(96)00041-6.
Peters, H., and W. E. Johns (2005), Mixing and entrainment in the Red Sea outflow plume. Part II: Turbulence characteristics, *J. Phys. Oceanogr.*, *35*, 584–600, doi:10.1175/JPO2689.1.
Rimoldi, B., J. Alexander, and S. Morris (1996), Experimental turbidity currents entering density stratified water: Analogues for turbidities in Mediterranean hypersaline basins, *Sedimentology*, *43*, 527–540, doi:10.1046/j.1365-3091.1996.d01-21.x.
Rodi, W. (1993), *Turbulence Models and Their Application in Hydraulics*, A. A. Balkema, Rotterdam, Netherlands.
Samothrakis, P., and A. J. Cotel (2006a), Propagation of a gravity current in a two-layer stratified environment, *J. Geophys. Res.*, *111*, C01012, doi:10.1029/2005JC003125.
Samothrakis, P., and A. J. Cotel (2006b), Finite volume gravity currents impinging on a stratified interface, *Exp. Fluids*, *41*, 991–1003, doi:10.1007/s00348-006-0222-x.
Sequeiros, O., B. Spinewine, R. T. Beaubouef, T. Sun, M. H. García, and G. Parker (2010), Characteristics of velocity and excess density profiles of saline underflows and turbidity currents flowing over a mobile bed, *J. Hydraul. Eng.*, *136*, 412–433, doi:10.1061/(ASCE)HY.1943-7900.0000200.
Sequeiros, O. E. (2012), Estimating turbidity current conditions from channel morphology: A Froude number approach, *J. Geophys. Res.*, *117*, C04003, doi:10.1029/2011JC007201.
Strang, E. J., and H. J. S. Fernando (2001), Vertical mixing and transports through a stratified shear layer, *J. Phys. Oceanogr.*, *31*, 2026–2048, doi:10.1175/1520-0485(2001)031<2026:VMATTA>2.0.CO;2.
Talling, P. J., C. K. Paull, and D. J. Piper (2013), How are subaqueous sediment density flows triggered, what is their internal structure and how does it evolve? Direct observations from monitoring of active flows, *Earth Sci. Rev.*, *125*, 244–287, doi:10.1016/j.earscirev.2013.07.005.
Turner, J. S. (1986), Turbulent entrainment: The development of the entrainment assumption and its application to geophysical flows, *J. Fluid Mech.*, *173*, 431–471, doi:10.1017/S0022112086001222.
Venayagamoorthy, S. K., and O. B. Fringer (2007), On the formation and propagation of nonlinear internal boluses across a shelf break, *J. Fluid Mech.*, *577*, 137–159, doi:10.1017/S0022112007004624.
Venayagamoorthy, S. K., and O. B. Fringer (2012), Examining breaking internal waves on a shelf slope using numerical simulations, *Oceanography*, *25*, 132–139, doi:10.5670/oceanog.2012.48.
Wang, B., S. N. Giddings, O. B. Fringer, E. S. Gross, D. A. Fong, and S. G. Monismith (2011a), Modeling and understanding turbulent mixing in a macrotidal salt wedge estuary, *J. Geophys. Res.*, *116*, C02036, doi:10.1029/2010JC006135.
Wang, R. Q., A. Law, E. E. Adams, and O. B. Fringer (2011b), Large-eddy simulation of starting buoyant jets, *Environ. Fluid Mech.*, *11*(6), 591–609, doi:10.1007/s10652-010-9201-0.
Warner, J. C., C. R. Sherwood, H. G. Arango, and R. P. Signell (2005), Performance of four turbulence closure models implemented using a generic length scale method, *Ocean Modell.*, *8*, 81–113, doi:10.1016/j.ocemod.2003.12.003.
Wells, M. G., and P. Nadarajah (2009), The intrusion depth of density currents flowing into stratified water bodies, *J. Phys. Oceanogr.*, *39*, 1935–1947, doi:10.1175/2009JPO4022.1.
Wells, M. G., and J. S. Wettlaufer (2007), The long-term circulation driven by gravity currents in a two-layer stratified basin, *J. Fluid Mech.*, *572*, 37–58, doi:10.1017/S0022112006003478.
Wells, M. G., C. Cenedese, and C. P. Caulfield (2010), The relationship between flux coefficient and entrainment ratio in density currents, *J. Phys. Oceanogr.*, *40*, 2713–2727, doi:10.1175/2010JPO4225.1.
Wobus, F., G. I. Shapiro, J. M. Huthnance, and M. A. M. Maqueda (2013), The piercing of the Atlantic Layer by an Arctic shelf water cascade in an idealized study inspired by the Storfjorden overflow in Svalbard, *Ocean Modell.*, *71*, 54–65, doi:10.1016/j.ocemod.2013.03.003.
Zang, Y., R. L. Street, and J. R. Koseff (1993), A dynamic mixed subgrid-scale model and its application to turbulent re-circulating flows, *Phys. Fluids A*, *5*, 3186–3196, doi:10.1063/1.858675.
Zang, Y., R. L. Street, and J. R. Koseff (1994), A non-staggered grid, fractional step method for time-dependent incompressible Navier–Stokes equations in curvilinear coordinates, *J. Comput. Phys.*, *114*, 18–33, doi:10.1006/jcph.1994.1146.
Zedler, E. A., and R. L. Street (2001), Large-eddy simulation of sediment transport: Currents over ripples, *J. Hydraul. Eng.*, *127*, 442–452, doi:10.1061/(ASCE)0733-9429(2001)127:6(444).
Zedler, E. A., and R. L. Street (2006), Sediment transport over ripples in oscillatory flow, *J. Hydraul. Eng.*, *132*(2), 1–14, doi:10.1061/(ASCE)0733-9429(2006)132:2(180).